Post-Print of: Journal of Alloys and Compounds Volume 536, Supplement 1, 25 September 2012, Pages S398–S406

International Symposium on Metastable, Amorphous and Nanostructured Materials, ISMANAM-2011 (26th June to July 1st 2011)

Microstructural characterization of hydrophobic Ti1−xAlxN coatings with moth-eye-like surface morphology

V. Godinho (a), C. Lopez-Santos (b), T.C. Rojas (a), D. Philippon (a), M.C. Jimenez de Haro (a), S. Lucas (b), A. Fernandez (a)

(a) Instituto de Ciencia de Materiales de Sevilla CSIC-Uni. Sevilla, Av. Americo Vespucio 49, 41092 Sevilla, Spain

(b) NAmur Research Institute for LIfe Sciences (NARILIS), Research Center in Physics of Matter and Radiation (PMR), University of Namur (FUNDP), 61 Rue de Bruxelles, 5000 Namur, Belgium

Abstract

Ti1−xAlxN thin films with different Al content were deposited by magnetron sputtering. The combination of electron energy loss spectroscopy (EELS) and energy dispersive spectroscopy (EDS) was used to evaluate the composition of the coatings. The effect of Al content on the morphology and properties of the coatings was investigated. High resolution electron microscopy and related techniques revealed the formation of a pillared moth-eye-like nanostructure with variable size and distribution of meso- and nano-columns and different degree of open porosity that depends on the Al content on the coating. For low Al content ($x \leq 0.21$) c-(Ti,Al)N highly porous columns ending in a sharp pyramidal shape present low reflectivity and high hydrophobicity. While the precipitation of h-AlN phase at the column boundaries for $x = 0.71$ suppresses the c-(Ti,Al)N columnar growth and produces a smother surface, with higher reflectivity and less hydrophobic character.

Keywords

Ti1−xAlxN coatings; Moth-eye-like structure; EELS; HAADF/STEM; Antireflective; Hydrophobic

1. Introduction

In the recent years the field of application of Ti1−xAlxN coatings has spread from the traditional mechanical cutting tools [1] to electronic devices [2], solar selective applications [3], [4] and [5] and even to satellite industry [6] and [7]. The optical properties of these Ti1−xAlxN coatings can be tuned in a wide range from metallic to dielectric character by controlling the stoichiometry x. In particular, these coatings are widely used in selective infrared (IR) applications like solar-control windows where a high color-neutral transmittance in the visible (VIS), good reflectance at the near-infrared and low thermal emittance are important properties [5]; solar absorber collectors with high absorptance in the solar spectrum and low thermal emittance in the IR [8]; and satellite temperature control coatings where the balance between solar absorptance and thermal emittance is crucial to control the temperature,

decreasing the absorptance and increasing the emittance of the coatings an equilibrium temperature for the satellite can be achieved [6].

The typical morphologies of TiAlN coatings deposited under low energetic conditions, composed of columns in the growing direction, ending in a pyramidal shape (in the 100 nm range) have been reported as a good strategy for obtaining antireflective coatings [9] and [10]. These structures mimic the eyes and wings of certain species of moth which are covered by tapered pillars smaller than the wavelength of incident light suppressing the reflection of light at wavelengths from the ultraviolet to mid-infrared [11].

In addition, the nanoscale hierarchical structures of the TiAlN coatings produced under different deposition conditions, generate coatings with different surface free energy and wetting properties [12] whose control is of interest for the above mentioned applications; namely for solar-control windows or solar absorbers. The partial pressure of nitrogen during deposition is reported to affect the morphology of Ti1−xAlxN coatings; an increase in the N2 fraction produces a decrease of surface roughness for similar power supplied to the targets [7] and [13].

From the microstructural point of view, the effect of continuously adding Al to the TiN lattice has been widely studied by many authors [14], [15], [16] and [17]. There is a general consent that for low Al content, a single phase solid solution c-(Ti,Al)N is present while for higher Al content a dual-phase structure of c-(Ti,Al)N and h-AlN can be found, a further increase in the Al amount leads to a single phase h-AlN. The limits of these regions are not always the same for the different authors [3] and it is also possible that the deposition parameters play a major role on the microstructure and the limits of each phase [15].

In this work we report how by changing a set of deposition conditions, coatings with different morphologies and compositions can be prepared by magnetron sputtering. In particular, the effects of Al content on the reflectance spectra and wettability of the coatings are investigated. The microstructure of coatings with different Al content is deeply investigated using electron microscopy techniques and related with the different properties presented by the coatings. Previous papers [5], [6], [7] and [9] investigated different aspects of this complex system focusing mainly on compositional changes and reflectivity measurements. The interest of the present paper is to focus, not only on the composition vs. reflectivity (in a wide range from VIS to far IR), but to demonstrate that morphological/microstructural characteristics can also be related to the measured macroscopic reflectivity and hydrophobicity properties. The tailored combination of the properties and microstructure in a wide range of compositions is of high interest for potential applications in solar-control windows [5] or solar-absorber collectors [8].

2. Experimental

Fig. 1 shows a schematic diagram of the deposition chamber used and Table 1 summarizes the synthesis conditions for the Ti1−xAlxN coatings studied in this work. Pure Ti and pure Al targets were used (Kurt Lesker 99.99%) under dc discharge. The deposition took place in several steps, starting with an argon atmosphere and increasing gradually the nitrogen partial pressure, keeping the total pressure in the chamber constant (see Table 1). In Table 1 the nitrogen percentage corresponds to the nitrogen partial pressure in the gas phase for each step keeping the total pressure (N2 + Ar) at 1.33 Pa. No substrate bias or additional heating was applied during deposition (deposition temperature was ∼120 °C). The purpose is to obtain Ti1−xAlxN coatings with different x and different structure.

The coatings were deposited on AISI 316 steel, sodium chloride and silicon (1 0 0) substrates.

Scanning electron microscopy with field emission gun (SEM-FEG) was performed to study the morphology and thickness of samples in a high resolution microscope, HITACHI S4800. The samples were cleaved from coatings grown onto silicon, and were observed without metallization in cross sectional views at 1–2 kV.

The surface roughness (root mean square roughness—rms roughness) was evaluated using a Mahr "stylus" profilometer (conic stylus dimension of 2 μm with a lateral resolution of 0.76 nm) along a 7.5 mm profile.

The structure of these coatings was investigated by grazing incidence X-ray diffraction and selected area electron diffraction. The grazing incidence X-ray diffraction (GIXRD) equipment used was a Siemens D5000 (Cu Kα radiation). For GIXRD analysis samples deposited on silicon substrates were used.

A Philips CM200 transmission electron microscope (TEM) equipped with a parallel detection electron energy loss spectroscopy (EELS) spectrometer from Gatan (766-2 kV) was used. For TEM analysis thin foils were prepared from cross-sectioned slices of coatings deposited on silicon (1 0 0), by mechanical polishing followed by argon ion milling to electron transparency. Also planar view samples were prepared from samples deposited on sodium chloride substrates, which were floated off in distilled water and supported on a TEM copper grid. Electron energy-loss spectroscopy and X-ray energy dispersive spectroscopy (EDS) were used on the TEM to analyze the composition of the films in the cross-section. Selected area electron diffraction (SAED) was used to investigate the formation of crystalline phases in the nanoscale.

High-angle annular dark field in a scanning transmission electron microscopy (HAADF-STEM) and EELS spectra obtained by the spectrum-imaging mode were recorded on a JEOL JEM-2010F working at 200 KeV. The signal intensity of the HAADF-STEM images is proportional to the atomic number and the thickness of the sample on the analyzed area. The spectrum imaging mode, consisting in acquiring a series of EELS spectra while a 0.5 nm beam scanned along the sample area, was used. The HAADF signal was simultaneously collected at each point within the scanned area. This approach allows correlating nanoanalytical and structural information of the region under study.

Samples surface composition was investigated by X-ray photoelectron spectroscopy (XPS). The XPS equipment was a Leybold Heraus Spectrometer working in the constant analyzer energy mode with a pass-energy of 50 eV. The samples were analyzed with Mg Kα radiation. The binding energy reference was taken as the main component of the C1s peak at 284.6 eV for a mixture of adventitious and pure carbon.

Near IR and IR reflectivity measurements in the spectral range of 0.8–1.1 and 1.3–200 μm respectively, have been done using IFS 66v/s (BRUKER) infrared Fourier-transform spectrometer with reflection units at the near normal incidence and at the oblique angles of incidence up to the grazing angles (reflection–absorption spectroscopy (RAS)) in polarized light for samples grown on steel substrates. The spectral resolution was 4 cm−1.

In the visible range (0.4–0.8 μm) the coatings total reflectance was measured in a Shimadzu UV-2101PC spectrometer equipped with an integrating sphere. Barium sulphate was used as reference. The measurements were performed on coated steel substrates (AISI 316).

Hydrophobicity analysis was performed through static water contact angle measurements with OCA20 equipment and SCA20 software (Dataphysics). Bidistilled water sessile drops of 1 µl were employed. The reported values are an average of ten measurements taken for each examined surface of coatings deposited on silicon. In a similar way, contact angles of iodomethane were also measured to estimate the polar and non-polar contributions to the surface tension by the Owens–Wendt–Kaelble approximation [18].

3. Results and discussion

On Table 2 the chemical composition of the coatings given by EELS and EDS is presented. EELS spectra, N and O K-edges and Ti L2,3-edge, were registered on coatings cross-section, and these data together with EDS data (of Ti and Al) were used to determine the chemical composition of the samples. By controlling the deposition parameters samples with different stoichiometry x of Ti1−xAlxN were obtained. However, the coatings are composed, not only of Ti, Al and N, also an O contamination (from 5 to 22 at%) was found. Due to the vacuum conditions and the high reactivity of Ti and Al toward oxygen it is not possible to exclude the incorporation of oxygen in the films during deposition under our experimental conditions, in particular for lower depositions rates (see deposition rates in Table 1) [19]. In addition as we will discuss below, the desired columnar microstructure of these films for promoting low reflectivity and high hydrophobicity, will also influence the post-deposition incorporation of oxygen.

Similar x values for Al content were found by XPS. However, surface analysis techniques as XPS are not appropriate for the characterization of chemical composition of coatings composed of elements with high affinity to oxygen due to its readily oxidation when exposed to air.

The crystalline phases formed were evaluated by GIXRD. Fig. 2 shows the different diffraction patterns of these samples. The diffraction peaks are between those of cubic TiN and cubic TiAlN. As the Al content increases there is a displacement in the diffraction peaks to higher 2θ. Adding gradually Al to the cubic TiN phase leads to an increase of the crystalline phase and a decrease of lattice parameters caused by the substitution of Ti atoms by Al atoms with smaller atomic radius; shifting the 2θ peaks in Ti1−xAlxN to higher values as compared to TiN. The highest Al content leads to the appearance of a small peak at 2θ = 66° that could be associated with the presence of h-AlN phases.

No crystalline oxide phases were found. The high oxygen contamination is probably leading to the formation of amorphous oxide or oxynitride phases of Ti and Al.

The phases formed were also analyzed by SAED. Fig. 3 presents the results as a function of the Al content in the films. For Al contents lower than x = 0.59 a single cubic (Ti,Al)N (c-(Ti,Al)N) phase is present. At x = 0.59 an hexagonal AlN (h-AlN) phase co-exists with the c-(Ti,Al)N phase. These results are in agreement with Zhou et al. [15] that define a region between x = 0.6 and x = 0.7 where it is possible to find both phases, while below and above these limits only c-(Ti,Al)N and h-AlN phases are respectively found.

The bonding structure of the coatings was evaluated by EELS inside the TEM. Fig. 4(a) presents in detail the N K-edge. The spectra are similar to those presented by MacKenzie et al. [20] for TiAlN coating, and show clear differences in the N K-edge with the increase of Al content. The introduction of Al in the c-TiN phase increases the second resonance of the N K-edge, while the first resonance decreases. The continuous increase in Al leads to the precipitation of the h-AlN phase that produces broadening of the second resonance and the disappearance of the first resonance.

According to MacKenzie et al. [20] the EELS spectra of c-(Ti,Al)N should be a linear combination of c-TiN and c-AlN spectra. In this sense, using the reference spectra of c-TiN, c-AlN and h-AlN, the N K-edges of the Ti1−xAlxN coatings were calculated taking into account the different compositions and the SAED results for the different phases formed. Fig. 4(b) shows the results. The linear combinations were performed assuming that all Ti in the coating was in the form of c-(Ti,Al)N. When there is an excess of Al, this excess is in the form of h-AlN giving rise to the coexistence of the two phases as demonstrated by TEM-SAED. The calculated spectra are in good agreement with the experimental results, and the method is presented here as good way to predict experimental results.

However, not only composition is influencing the properties of the coatings, the surface morphology of TiAlN coatings is very important in what concerns their wettability and its application as antireflective coatings. The nitrogen partial pressure during deposition is reported to affect the surface roughness of Ti1−xAlxN coatings [7] and [13], but the effects of Al content on surface roughness have been also reported [12]. In this work we focus on the study of the effect of the different Al content on the morphology and microstructure of the coatings deposited under similar nitrogen pressure. In particular, Fig. 5 shows in detail the different morphologies obtained by SEM-FEG cross-sectional and planar views for the selected samples with x = 0.07, 0.21 and 0.71.

A columnar growth typical of samples grown under low adatom mobility as described by Zone 1 of Thornton's diagram is observed [21]. The different power ratios applied under the same nitrogen pressure give rise to different structures. In general all samples present a columnar structure constituted by “meso-columns” (understanding that meso is between micro and nano) which are formed by aggregates of smaller columns (“nano-columns”). It is possible to see the voids between the meso-columns.

For very low Al content the c-(Ti,Al)N meso-columns (150–200 nm wide) are formed by nano-columns with open spaces between them, which grow tilted in respect to the direction of the meso-columns. A competitive growth of the nano-columns in all directions results in a peculiar “fractalish cauliflower” structure with pyramidal ending.

When the same power is applied to both targets (x = 0.21) the competitive growth of the nano-colums is suppressed. The nano-columns grow parallel to each other in an ordered way. The meso-columns of 70–90 nm end in triangular pyramids typical of c-(Ti,Al)N coatings [5], [7] and [12].

For x = 0.71 the meso-columns are now formed by nano-columns in the growing direction with globular ending, resulting in a compact structure with a cauliflower look surface. The increase of the power supplied to the Al targets produces an excess of Al, that precipitates in an h-AlN phase which interrupts the c-(Ti,Al)N columnar growth originating in a smoother surface [7]. High resolution transmission electron micrograph (on coating's cross-section) in the inset of Fig. 6 revealed that the hexagonal AlN phase, characterized by an interplanar distance of 2.7 Å, precipitates at the nano-column boundaries. Also the characteristic 2.4 Å interplanar distance corresponding to cubic TiAlN phase is observed. As observed for the planar observations the SAED pattern corresponds to a mixture of c-(Ti,A)N and h-AlN phase.

As one could expect, the high oxygen contamination observed can also be due to the columnar structure and the open voids between and inside the meso-columns. In particular, samples TiAlN(O)/200–200 and TiAlN(O)200–400 with x = 0.21 and x = 0.59 respectively, present

oxygen contents of 22 and 13 at%. The microstructure of these coatings was investigated in more detail by cross-sectional TEM (XTEM). In Fig. 7(a) and (b) the columnar structure of these samples can be observed in more detail both by SEM and TEM. Sample with higher Al content (x = 0.59, Fig. 7(a) presents meso-columns from 100 to 150 nm wide ending in pyramids of ∼20 nm height. From the TEM micrograph it is possible to see the abrupt columns with intra-columnar voids. Inside the columns, a superlattice microstructure with a period of 8 nm can be seen. This corresponds to the nano-columns growing tilted with respect to the growing direction. The columns are formed by c-(Ti,Al)N with the precipitation of h-AlN at columns boundaries as indicated by the SAED pattern, corresponding to the co-existence of both phases. In this case the amount of h-AlN (estimated at around 18% from the EELS linear combination) phase is not sufficient to interrupt the growth of the typical c-(Ti,Al)N structure as observed in the sample with the higher Al content (with an h-AlN contribution of 42% according to the EELS results).

For lower Al content (x = 0.21, Fig. 7(b) the columns are narrower, but from the contrasts in the XTEM image, a similar superlattice structure of the small nano-columns tilted in respect to the film growing direction is observed. In the HAADF-STEM image the darker areas, corresponding to the pores between the tilted nano-columns, are found to follow the same pattern. The EELS analysis inside and outside the pores, is presented in Fig. 7(b). No appreciable changes are observed for the N K and Ti L2,3-edges. However, inside the pores there is a significant increase of the O K-edge. The highly porous structure, with open pores is therefore the reason for the high oxygen content measured by EELS in these coatings cross-section.

The optical properties of the different structures in Fig. 5 with sub-wavelength scale features were investigated. Moth-eye-like antireflecting coatings play an important role in a wide variety of optical technologies by reducing reflective loss at interfaces. Fig. 8 presents the reflectivity of these coatings in the spectral range from 0.4 to 0.8, 0.8–1.1 and 1.3–200 μm. The three coatings present very low reflectivity (<0.3) up to 1.1 μm. The sharp and regular moth-eye-like structure of the coating with x = 0.21 is responsible for the lower reflectivity spectrum.

For wavelengths higher than 1.3 μm the reflectivity of the coatings increases, being similar to TiN in the case of x = 0.21. The high thickness of x = 0.07 causes interference effects, that can be used to control the solar selective response of the coatings in particular to reduce the equilibrium temperature.

The wetting properties of these coatings were also tested. Table 3 presents the results of static water contact angle and surface energy. Ti1−xAlxN coatings show a notable hydrophobic character, with water contact angles around 110°. However, it is possible to observe slight differences between the wettability of these samples that could be attributed to differences on the developed microstructure and the surface chemical composition. In this case, the smoother and more compact sample with x = 0.71 (after the structural phase change with segregation of h-AlN), presents a smaller water contact angle. Meanwhile, an increase in the surface roughness, through the columnar growth of the cubic phase, provides more hydrophobic surfaces, as is the case of the samples with x = 0.07 and x = 0.21. This tendency is in agreement with the known effect of the roughness on the water contact angle proposed by the Wenzel model [22]. It is worth to mention that no direct correlation was found between the samples thickness and surface roughness (see the results on Table 1). Besides, previous works have presented similar water contact angles on similar Ti1−xAlxN morphologies [12].

Surface tension measurements confirm this result: the smoother coating (x = 0.71) has the lower surface tension.

The surface chemistry and bonding state of the elements were investigated by XPS. According to Fig. 9 of the nitrogen N1s XPS spectra, the contribution of different bonded species can be found on the Ti1−xAlxN surface. The peaks are broad and slightly shifted to higher binding energy compared to typical values reported for TiAlN coatings [23] (indicated in the figure by the marked area). The appearance of high binding energy shoulders is observed with a higher intensity for the sample with the higher Al content (x = 0.71). These bands are attributed to the contribution of Nsingle bondO surface bonds expected at 399.1 eV [23]. It appears that the sample with a higher Al content also shows a higher surface oxidation. According to the planar view images in Fig. 5 the sample with x = 0.71 shows a smoother surface formed by smaller grains separated by a clear porosity what makes oxygen more accessible to produce a higher surface oxidation. Therefore, the precipitation of the new h-AlN phase seems to generate a less hydrophobic character of the Ti1−xAlxN surface, with a smoother topography and a higher content of AlN and NO groups.

4. Conclusions

Ti1−xAlxN thin films with different composition and structure were deposited by magnetron sputtering. The influence of Al content on the microstructure and phase formation has been investigated by XRD, SAED, TEM and SEM-FEG. The co-existence of h-AlN, and c-(Ti,Al)N phase, was detected by SAED and confirmed by EELS linear combinations for $x \geq 0.59$. The high resolution TEM study showed that the h-AlN phase precipitates at the column boundaries.

The detailed microstructural analysis in the nanoscale by high resolution SEM and TEM revealed the formation of a pillared moth-eye-like nanostructure with variable size and distribution of meso- and nano-columns depending on the deposition conditions. For the same nitrogen pressure different morphologies were obtained in function of the Al content. For higher Al content, the precipitation of the h-AlN phase at the columns boundaries suppresses the growth of the c-(Ti,Al)N phase and a smother surface is obtained.

HAADF and STEM/EELS analysis, revealed that the oxygen content in the coatings is mainly due to the presence of a highly porous columnar structure. The EELS measurements inside and outside the pores indicate higher oxygen content inside pores proving that the porosity is open contributing to post-deposition oxidation in the coating.

The reflectance spectra show that these coatings present very low reflectivity in particular for columnar structures with sharp pyramidal edges. This structure also favors the hydrophobic character presented by all coatings. The combination of all the results reported in this paper allow us to propose the TiAlN coatings as very interesting hydrophobic materials for infrared selective applications. The method of preparation is simple and morphology and chemical composition can be tuned easily by varying the deposition conditions. In this paper we showed how the promotion of columnar structures (for low IR reflectivity and hydrophobicity applications) can be easily combined with a wide range of compositions what allow also to tune the electrical properties from metallic (TiN) to dielectric (AlN) character.

Acknowledgments

Authors thank the financial support from EC (REGPOT AL-NANOFUNC), CSIC (201060I41 and 201060E102), Spanish Ministry MICINN (Consolider FUNCOAT) and Junta de Andalucía.

References

[1] K.D. Bouzakis, G. Skordaris, N. Michailidis, I. Mirisidis, G. Erkens, R. Cremer

Surf. Coat. Technol., 202 (2007), pp. 826–830

[2] T.H. Cha, D.G. Park, T.K. Kim, S.A. Jang, I.S. Yeo, J.S. Roh, J.W. Park

Appl. Phys. Lett., 81 (2002), pp. 4192–4194

[3] V. Godinho, D. Philippon, T.C. Rojas, N.N. Novikova, V.A. Yakovlev, E.A. Vinogradov, A. Fernandez

Solar Energy, 84 (2010), pp. 1397–1401

[4] H.C. Barshilia, N. Selvakumar, K.S. Rajam, D.V.S. Rao, K. Muraleedharan, A. Biswas

Appl. Phys. Lett., 89 (2006)

[5] A. Schuler, V. Thommen, P. Reimann, P. Oelhafen, G. Francz, T. Zehnder, M. Duggelin, D. Mathys, R. Guggenheim

J. Vac. Sci. Technol. A-Vac. Surf. Films, 19 (2001), pp. 922–929

[6] M. Brogren, G.L. Harding, R. Karmhag, C.G. Ribbing, G.A. Niklasson, L. Stenmark

Thin Solid Films, 370 (2000), pp. 268–277

[7] J.T. Chen, J. Wang, F. Zhang, G.A. Zhang, X.Y. Fan, Z.G. Wu, P.X. Yan

J. Alloys Compd., 472 (2009), pp. 91–96

[8] K. Gelin, T. Boström, E. Wäcklegard

Solar Energy, 77 (2004), pp. 115–119

[9] F. Burmeister, C. Kohn, R. Kuebler, G. Kleer, B. Blasi, A. Gombert

Surf. Coat. Technol., 200 (2005), pp. 1555–1559

[10] F. Burmeister, E. Schaffer, G. Kleer, W. Doll, B. Blasi, A. Gombert

Surf. Coat. Technol., 200 (2005), pp. 1088–1092

[11] K.S. Liu, L. Jiang

Nano Today, 6 (2011), pp. 155–175

[12] V. Chawla, R. Chandra, R. Jayaganthan

J. Alloys Compd., 507 (2010), pp. L47–L53

[13] K. Chakrabarti, J.J. Jeong, S.K. Hwang, Y.C. Yoo, C.M. Lee

Thin Solid Films, 406 (2002), pp. 159–163

[14] J.C. Schuster, J. Bauer

J. Solid State Chem., 53 (1984), pp. 260–265

[15] M. Zhou, Y. Makino, M. Nose, K. Nogi

Thin Solid Films, 339 (1999), pp. 203–208

[16] T. Ikeda, K. Satoh

Thin Solid Films, 195 (1991), pp. 99–110

[17] T. Suzuki, Y. Makino, M. Samandi, S. Miyake

J. Mater. Sci., 35 (2000), pp. 4193–4199

[18] D.K. Owens, R.C. Wendt

J. Appl. Polym. Sci., 13 (1969), pp. 1741–1747

[19] J. Procházka, P. Karvánková, M.G.J. Veprek-Heijman, S. Veprek

Mater. Sci. Eng. A, 384 (2004), pp. 102–116

[20] M. MacKenzie, G.C. Weatherly, D.W. McComb, A.J. Craven

Scripta Mater., 53 (2005), pp. 983–987

[21] J.A. Thorton

Annu. Rev. Mater. Sci., 7 (1977), pp. 239–260

[22] R.N. Wenzel

Ind. Eng. Chem., 28 (1936), pp. 988–994

[23] J.C. Sanchez-Lopez, M.D. Alcala, C. Real, A. Fernandez

Nanostructured Mater., 11 (1999), pp. 249–257

Figure captions

Figure 1. Schematic diagram of the deposition chamber used.

Figure 2. XRD diffraction patterns of Ti1−xAlxN coatings with different Al contents.

Figure 3. SAED patterns of Ti1−xAlxN coatings with different Al contents.

Figure 4. (Left) Details of EELS N K-edge with reference spectra of c-TiN, c-AlN and h-AlN and (right) measured (solid lines) and simulated spectra (dashed lines) for the coatings with different Al content.

Figure 5. SEM-FEG micrographs presenting the morphology of the Ti1−xAlxN coatings (planar and cross-sectional views) prepared under 15% N2 fraction and different Al content.

Figure 6. XTEM micrograph of sample TiAlN(O)/200–600 with x = 0.71.

Figure 7. (a) Comparison of SEM-FEG and TEM micrographs presenting the morphology and details of the columns of sample TiAlN(O)/200–400 with x = 0.59. (b) Detail of the columns in sample TiAlN(O)/200–200 (x = 0.21) in XSEM-FEG and XTEM micrograph with corresponding SAED. HAADF/STEM image showing the presence of porosity and the corresponding EELS analysis inside and outside the pores.

Figure 8. Reflectance spectra of the Ti1−xAlxN coatings prepared under 15% N2 (TiAlN(O)/400–200 x = 0.07, TiAlN(O)/200–200, x = 0.21 and TiAlN(O)/200–600, x = 0.71).

Figure 9. N1s core level of XPS spectra of samples with different Al content (x = 0.07, 0.21 and 0.71) after A.

Table 1. Deposition conditions, thickness and surface roughness of the studied coatings.

Sample	**TiAlN(O)/200–200**			**TiAlN(O)/400–400**					**TiAlN(O)/200–400**			**TiAlN(O)/200–600**			**TiAlN(O)/400–200**		
Step	**1**	**2**	**3**	**1**	**2**	**3**	**4**	**5**	**1**	**2**	**3**	**1**	**2**	**3**	**1**	**2**	**3**
N_2% in gas phase	0	7	15	0	15	30	50	70	0	15	30	0	7	15	0	7	15
Dep. time (min)	10	10	130	5	5	5	5	130	10	10	130	5	5	140	5	5	140
Thickness (nm)	200[a]		1000[b]	340[a]				1700[b]	200[a]		1700[b]	50[a]		3650[b]	170[a]		4500[b]
Dep. rate (nm/min)	10		8	17				13	10		13	5		26	17		32
Target power (W)	Ti 200 W dc			Ti 400 W dc					Ti 200 W dc			Ti 200 W dc			Ti 400 W dc		
	Al 200 W dc			Al 400 W dc					Al 400 W dc			Al 600 W dc			Al 200 W dc		
rms Roughness (nm)	10			20					26			6			14		

a Underlayer.

b Coatings

Table 2. Chemical composition as given by combined EELS and EDS analysis (from TEM).

Sample	**EELS and EDS (at%)**				***x***	**1 − *x***
	Ti	**Al**	**N**	**O**		
TiAlN(O)/400–200	61	5	26	8	0.07	0.93
TiAlN(O)/200–200	39	11	28	22	0.21	0.79
TiAlN(O)/400–400	37	16	41	6	0.30	0.70
TiAlN(O)/200–400	21	29	37	13	0.59	0.41
TiAlN(O)/200–600	11	28	56	5	0.71	0.29

Table 3. Water contact angle (WCA) and surface energy (γ) polar (γ^p) and dispersive (γ^d).

Sample	***x***	**WCA (°)**	**γ (mN/m)**	**γ^p (mN/m)**	**γ^d (mN/m)**
TiAlN(O)/400–200	0.07	113.6	48.9	2.0	46.9
TiAlN(O)/200–200	0.21	116.4	64.5	5.0	59.5
TiAlN(O)/200–600	0.71	107.6	16.7	0.9	15.7

Figure 1

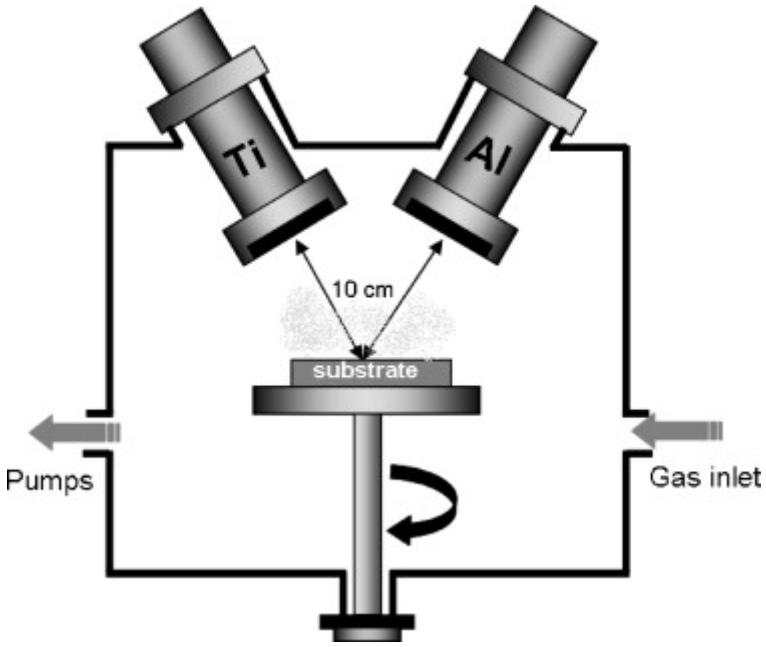

Figure 2

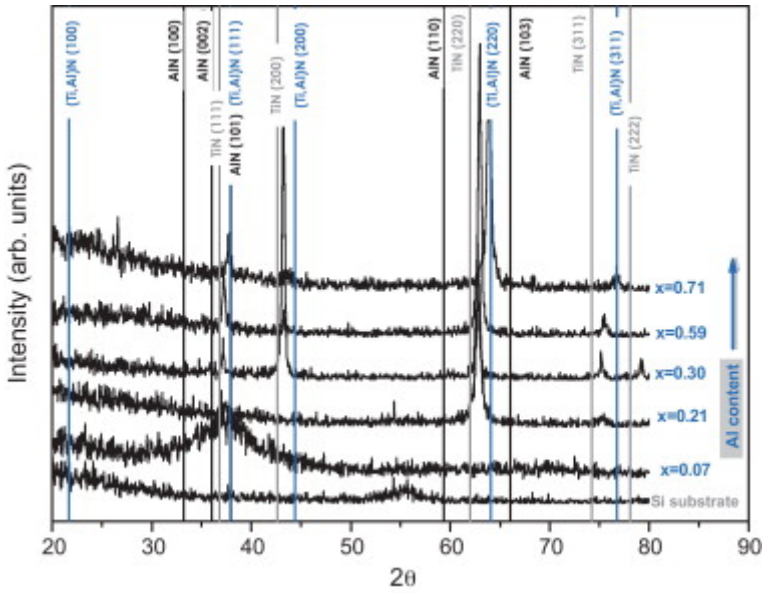
Intensity (arb. units)
2θ
20
30
40
50
60
70
80
90
(Ti,Al)N (100)
AlN (100)
AlN (002)
TiN (111)
(Ti,Al)N (111)
AlN (101)
TiN (200)
(Ti,Al)N (200)
AlN (110)
TiN (220)
(Ti,Al)N (220)
AlN (103)
TiN (311)
(Ti,Al)N (311)
TiN (222)
x=0.71
x=0.59
x=0.30
x=0.21
x=0.07
Si substrate
Al content

Figure 3

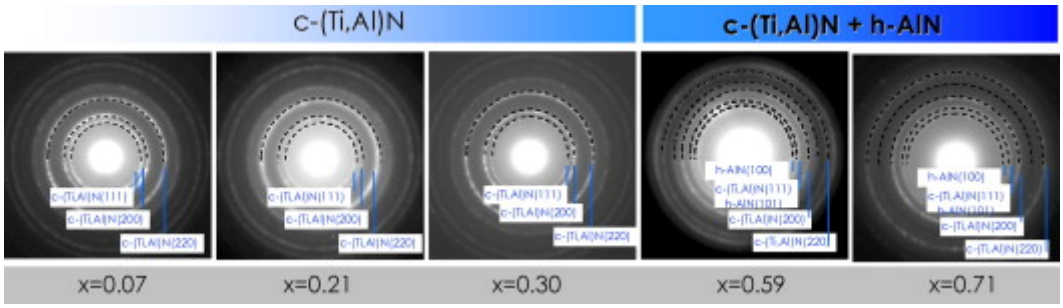

Figure 4

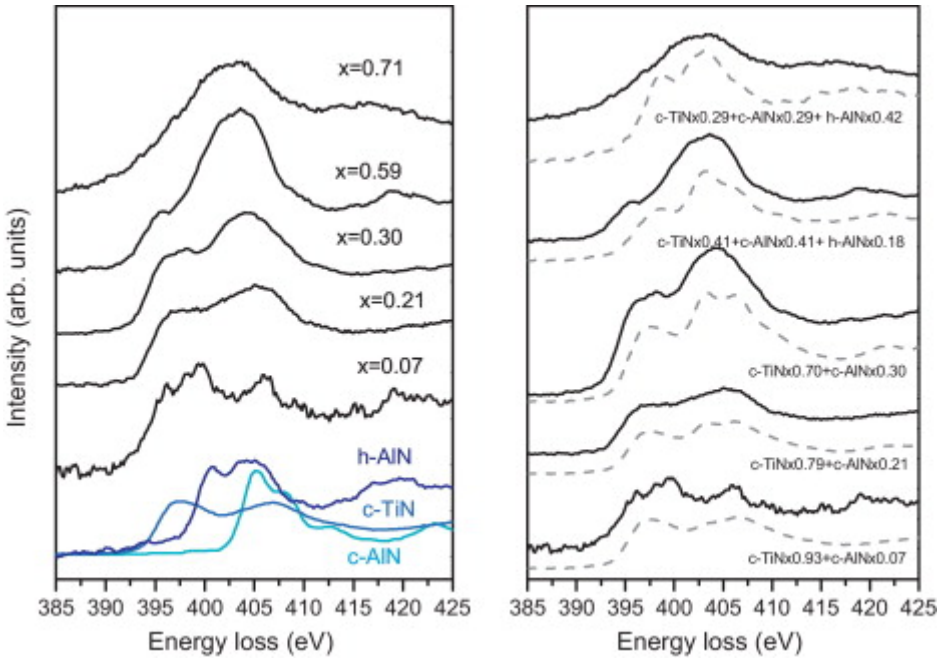
Intensity (arb. units)
x=0.71
x=0.59
x=0.30
x=0.21
x=0.07
h-AlN
c-TiN
c-AlN
385 390 395 400 405 410 415 420 425
Energy loss (eV)
c-TiNx0.29+c-AlNx0.29+ h-AlNx0.42
c-TiNx0.41+c-AlNx0.41+ h-AlNx0.18
c-TiNx0.70+c-AlNx0.30
c-TiNx0.79+c-AlNx0.21
c-TiNx0.93+c-AlNx0.07
385 390 395 400 405 410 415 420 425
Energy loss (eV)

Figure 5

(a) x=0.07

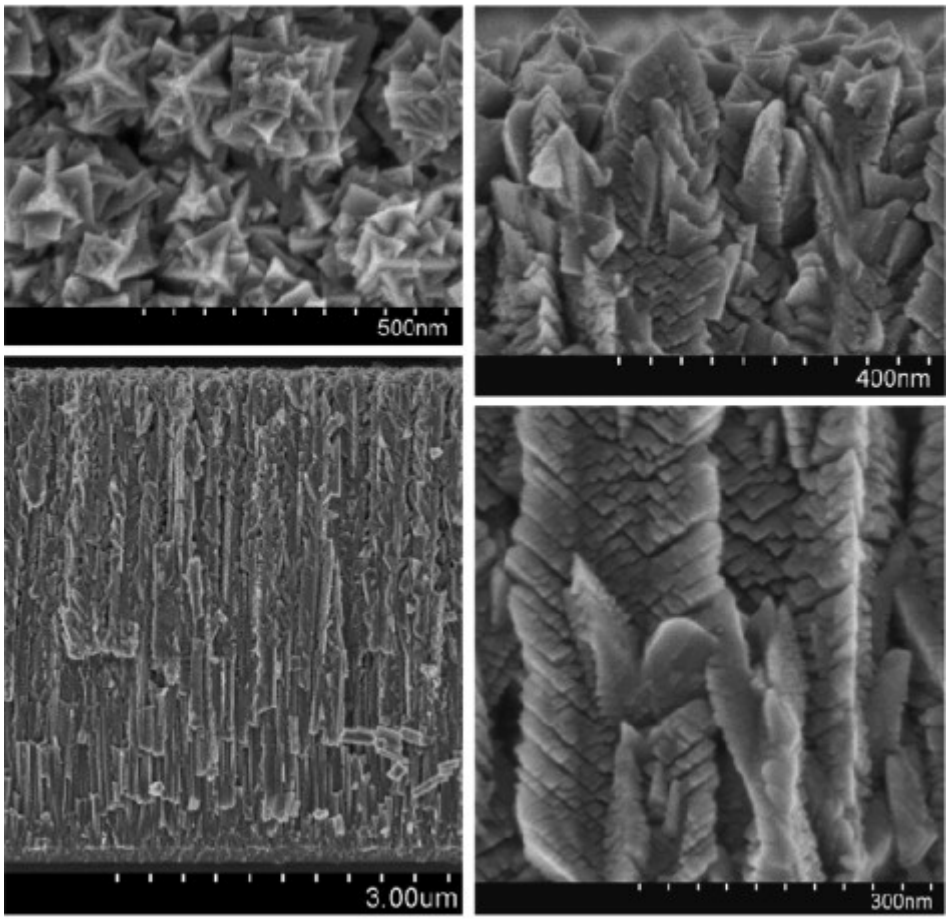

(b) x=0.21

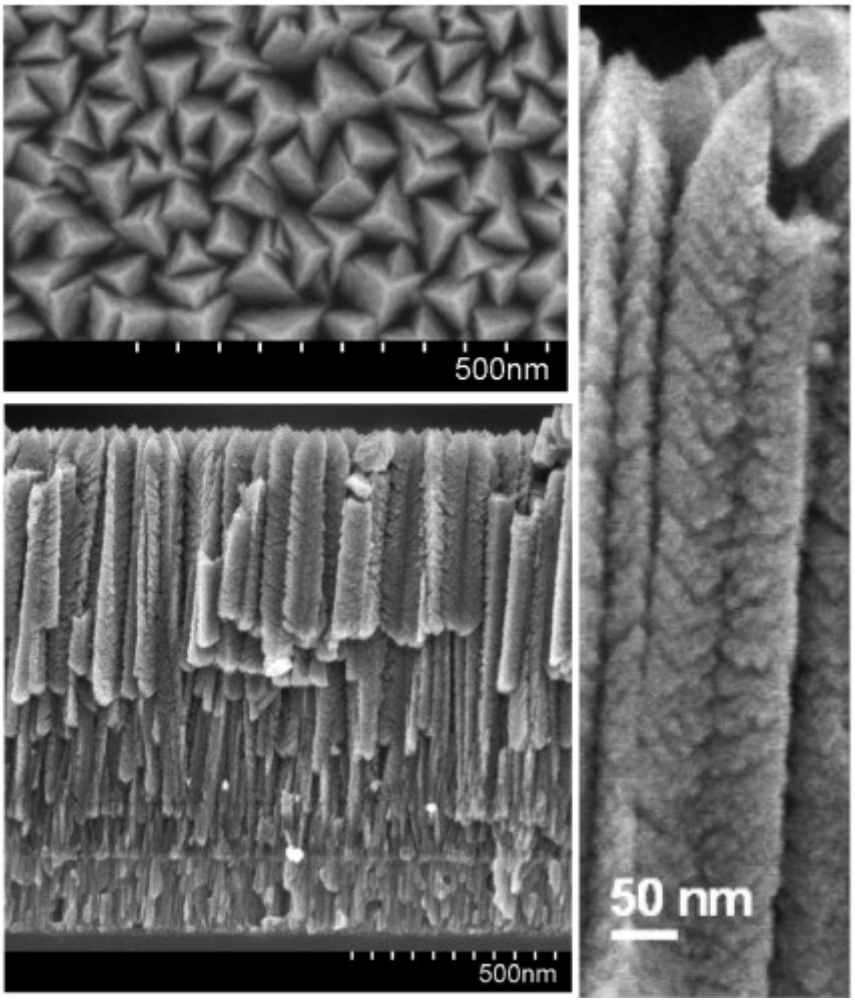

Figure 6

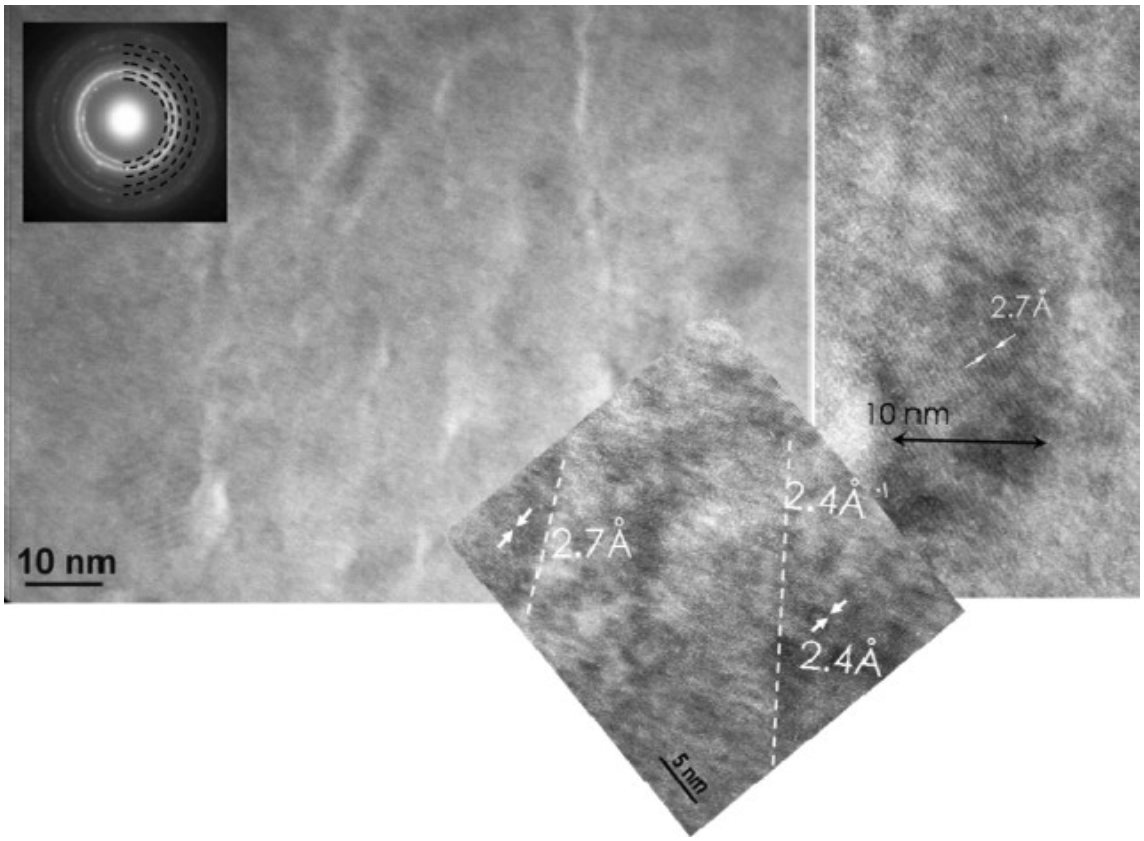

Figure 7

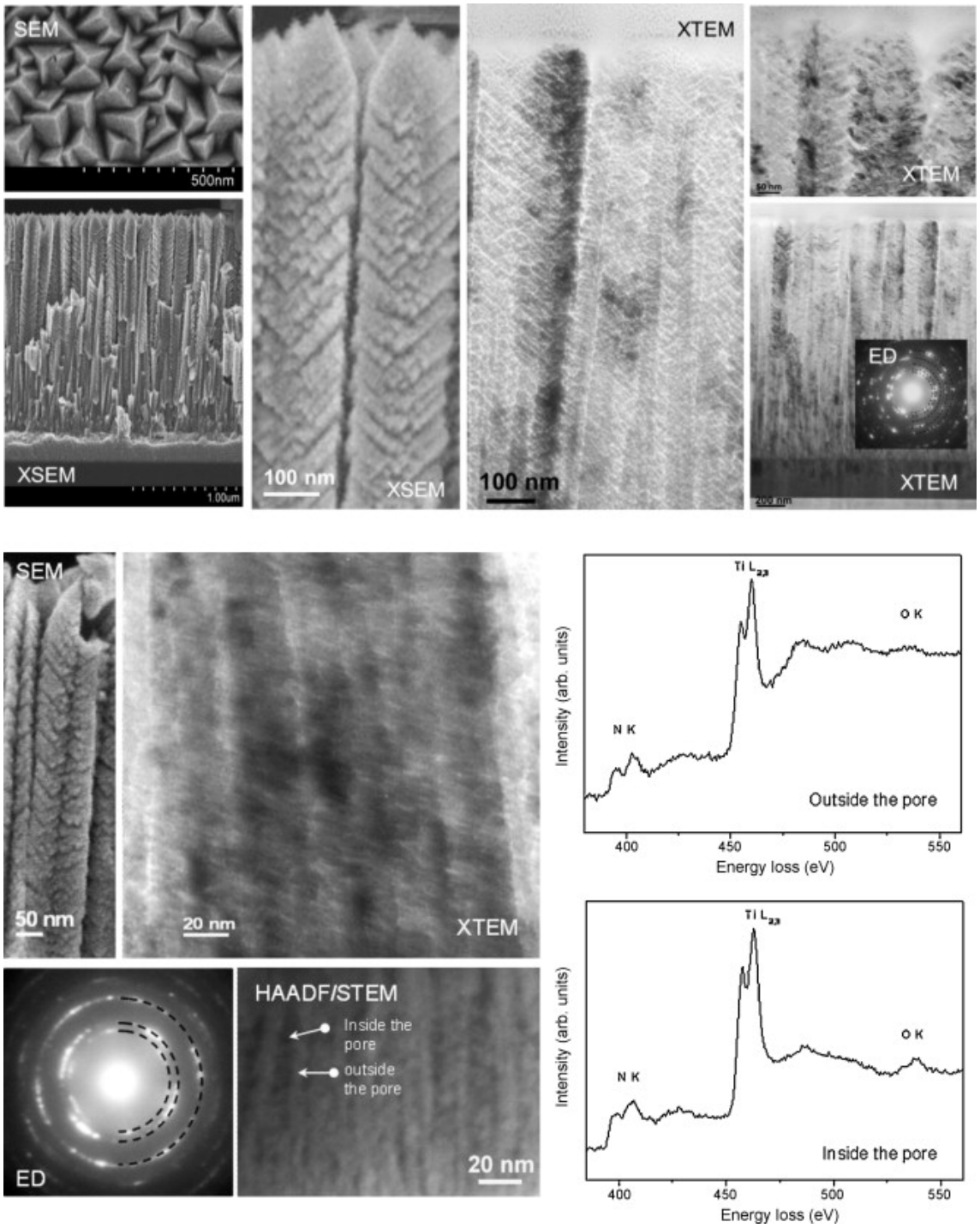
SEM
500nm
XSEM
1.00μm
100 nm
XSEM
XTEM
100 nm
XTEM
ED
XTEM
SEM
50 nm
20 nm
XTEM
ED
HAADF/STEM
Inside the pore
outside the pore
20 nm
Ti L23
O K
N K
Intensity (arb. units)
Outside the pore
400
450
500
550
Energy loss (eV)
Ti L23
O K
N K
Intensity (arb. units)
Inside the pore
400
450
500
550
Energy loss (eV)

Figure 8

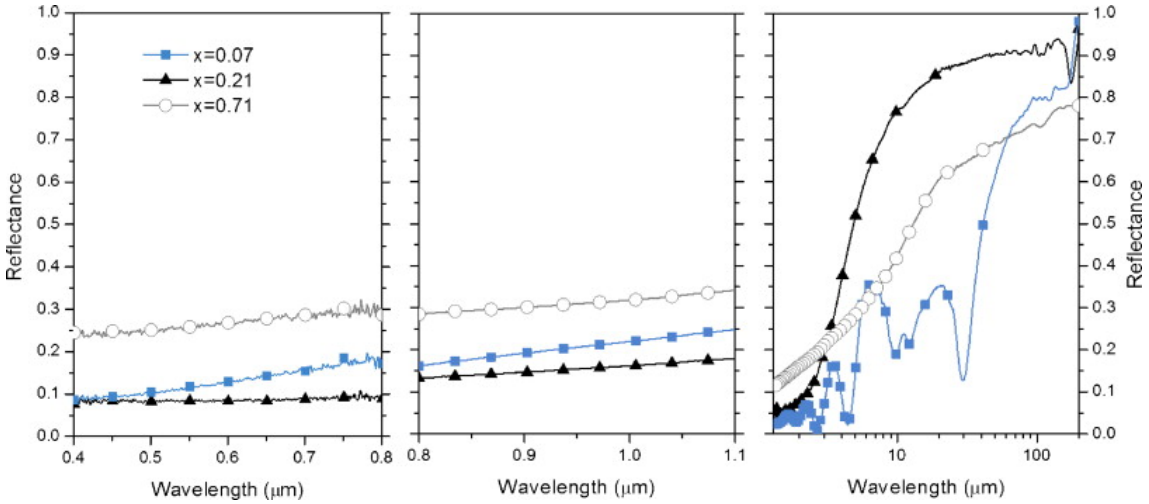
x=0.07
x=0.21
x=0.71
Reflectance
Wavelength (μm)
Wavelength (μm)
Wavelength (μm)
Reflectance

Figure 9

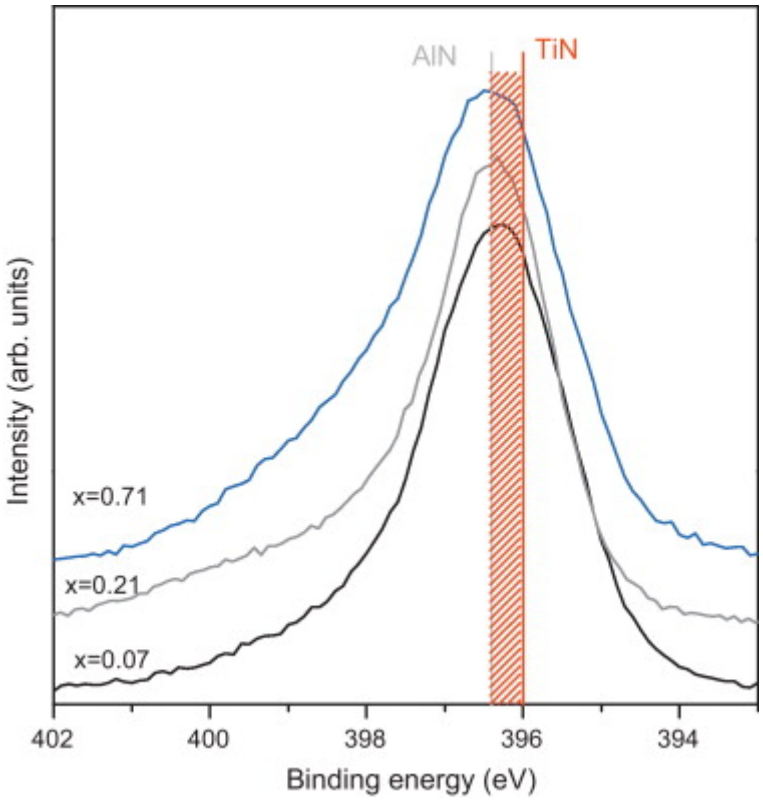
AlN
TiN
Intensity (arb. units)
x=0.71
x=0.21
x=0.07
402
400
398
396
394
Binding energy (eV)